applied sciences

MDPI

*Article*

# Effect of Heat Treatment on the Cavitation Erosion Behavior of Nanocrystalline Surface Layer of 304 Stainless Steel

**Nengliang Huang [1,2], Ye Tian [2], Rui Yang [2], Tonghu Xiao [1], Hua Li [2] and Xiuyong Chen [2,*]**

[1] School of Materials Science and Chemical Engineering, Ningbo University, Ningbo 315211, China; huangnengliang@nimte.ac.cn (N.H.); xiaotonghu@nbu.edu.cn (T.X.)
[2] Zhejiang-Japan Joint Laboratory for Antibacterial and Antifouling Technology, Zhejiang Engineering Research Center for Biomedical Materials, Cixi Institute of Biomedical Engineering, Ningbo Institute of Materials Technology and Engineering, Chinese Academy of Sciences, Ningbo 315201, China; tianye@nimte.ac.cn (Y.T.); yangrui@nimte.ac.cn (R.Y.); lihua@nimte.ac.cn (H.L.)
* Correspondence: chenxiuyong@nimte.ac.cn

**Abstract:** In this study, a nanocrystalline layer composed primarily of martensite phase was prepared on the surface of 304 stainless steel. Furthermore, the martensite phase content in the nanocrystalline layer was adjusted by heat treatment at 500 °C and 550 °C, respectively, and the cavitation erosion resistance of the nanocrystalline layer before and after heat treatment was investigated. The results showed that the nanocrystalline layer before and after heat treatment exhibited excellent erosion resistance, with cumulative mass loss of approximately 1/7, 1/5, and 1/3 that of the traditional 304 stainless steel, respectively. The nanocrystalline layer could significantly inhibit the growth of cavitation pits due to the high density of grain boundaries. However, due to the decrease in hardness of the nanocrystalline layer after heat treatment, the propagation speed of cavitation cracks was accelerated, and the cavitation erosion performance of the nanocrystalline layer showed a downward trend.

**Keywords:** 304 stainless steels; nanocrystalline layer; martensitic transformation; heat treatment; cavitation erosion

**Citation:** Huang, N.; Tian, Y.; Yang, R.; Xiao, T.; Li, H.; Chen, X. Effect of Heat Treatment on the Cavitation Erosion Behavior of Nanocrystalline Surface Layer of 304 Stainless Steel. *Appl. Sci.* **2023**, *13*, 5817. https://doi.org/10.3390/app13095817

Academic Editor: Chiara Soffritti

Received: 16 April 2023
Revised: 2 May 2023
Accepted: 6 May 2023
Published: 8 May 2023

**Copyright:** © 2023 by the authors. Licensee MDPI, Basel, Switzerland. This article is an open access article distributed under the terms and conditions of the Creative Commons Attribution (CC BY) license (https://creativecommons.org/licenses/by/4.0/).

## 1. Introduction

Cavitation erosion is a major cause of damage to fluid components, including turbine blades, propellers, pumps, and valves [1–5]. During the operation of these components, low-pressure zones form on their surfaces, resulting in the creation of cavitation bubbles [6]. The collapse of these bubbles due to pressure fluctuations generates shock waves/microjets that damage the surface of the material [7,8], significantly reducing the equipment's service life and increasing maintenance and operation costs. Strengthening the surface of the material is a feasible way to improve their cavitation erosion resistance, as surface damage is the primary mode of material damage. Researchers have conducted many studies on this topic [9–12]. They found that refining the surface grain size of materials to increase surface hardness effectively dissipates the energy generated by cavitation and greatly enhances cavitation erosion resistance [13].

Thapliyal et al. studied the cavitation erosion behavior of nickel–aluminum bronze after friction stir processing [14]. The initial grain size of the sample was around 190 μm, which was reduced to about 20 μm after treatment: a nearly 10-fold decrease. After cavitation erosion testing in a 3.5 wt % NaCl solution, the cavitation erosion resistance was greatly improved. Selvam et al. constructed a microstructured layer with an average grain size of 600 nm on the surface of austenitic stainless steel using friction stir welding [15]. After 20 h of cavitation erosion testing, the cumulative volume loss was only 16.7% of that of the original samples. Escobar et al. used friction stir processing to treat the surface of

S32205 duplex stainless steel, reducing the grain size of the austenite and martensite phases to 1 μm and 3 μm, respectively, resulting in a significant improvement in mechanical properties and a 70% reduction in cavitation erosion resistance compared to the original sample [16]. Although excellent cavitation erosion resistance was achieved through the microstructure refinement of the material surface and reduction in grain size, the grain size of the material was still relatively large and did not reach the nanometer scale (less than 100 nm). As is known, materials at the nanometer scale usually exhibit excellent mechanical properties [17]. Therefore, it is necessary to investigate whether refining the surface grain size of materials to the nanometer scale further enhances their cavitation erosion resistance.

Mechanical grinding technology has been proven to be used to prepare nanostructured layers on the surface of materials. Zhang et al. used surface mechanical grinding technology to prepare a layer of nanostructured layer on the surface of AISI 304 stainless steel [18]. The results showed that the nanocrystalline surface layer was mainly composed of martensitic phase, and the grain size was distributed between 8 and 60 nm. Thus, this study proposes using cutting-induced mechanical grinding to transform the austenitic phase in 304 stainless steel into martensitic phase with the aim of refining the surface microstructure to the nanometer level. In addition, the strain-hardening ability of martensite phase is low during cavitation erosion, which may be detrimental to cavitation erosion performance [19,20]. Therefore, in this study, it was also expected to further enhance the cavitation erosion resistance of the nanostructured layer by adjusting the content of austenitic and martensitic phases in the nanostructured layer through heat treatment.

## 2. Materials and Methods

### *2.1. Sample Preparation*

Commercially available 304 stainless steel (ϕ20 mm × 10 mm) was used in this study. The stainless steel was cut using a diamond saw blade (Dongguan Kechuang Grinding Materials Ltd., Dongguan, China) and a cutting machine (Brillant, ATM, Mammelzen, Germany). Then, a group of samples was polished with 50 nm $SiO_2$ suspension polishing solution for 10 min, which were denoted as 304-Nano samples. The other groups of samples were subjected to heat treatment at 500 °C and 550 °C using a 1700 °C vacuum atmosphere box furnace (SQFL-1700, Shanghai, China), respectively, and then ground with 3000 grit sandpaper for 1 min to remove the oxide layer. Finally, they were polished with 50 nm $SiO_2$ suspension polishing solution for 10 min and denoted as N-500 °C and N-550 °C, respectively. The samples that were only ground and polished were denoted as 304 samples.

### *2.2. Sample Characterization*

X-ray diffraction (XRD, D8 ADVANCE, Bruker, Saarbrucken, Germany) was used to analyze the phase composition with the voltage and current using 40 kV and 40 mA, and the calculation of martensite phase content and austenite phase content referred to previous reports [21]. Transmission electron microscopy (TEM, Talos F200x, ThermoFisher, Waltham, MA, USA) was used to characterize the microstructure, and the samples were prepared by focused ion beam (FIB, Auriga, Carl Zeiss, Oberkochen, Germany). A Vickers hardness test (Wilson VH3300, Buehler, Saarbrucken, Germany) was conducted by randomly selecting five points on the surface of the sample, applying a load pressure of 0.1 kgf. According to the modified testing standard ASTM G32 [22], the ultrasonic fatigue device (GBS-SCT 20 A, Guobiao Ultrasonic Equipment Co., Ltd., Hangzhou, China) was used to test the cavitation erosion resistance of the samples in deionized water. The working frequency was 20 kHz, and the amplitude was 50 μm. The oscillator was kept 23 ± 2 mm below the surface of the testing liquid, and the distance between the sample and the oscillator head was 1 mm. After each hour of cavitation erosion, the mass of the sample was weighed by an electronic analytical balance (METTLER 220, TOLEDO Instruments

Co., Ltd., Shanghai, China). A 3D optical profilometer (UP Lambda, Rtec Instruments Limited, San Francisco, USA) and SEM were used to observe the surface morphology of the sample after 15 h of cavitation erosion.

## 3. Results and Discussion

Figure 1 shows the TEM results of the nanocrystalline surface layer on 304 stainless steel. As shown in Figure 1A, the grain size clearly changed in a gradient manner, becoming finer closer to the surface. Furthermore, selected area electron diffraction (SAED) was performed on the region near the surface in Figure 1A, and the diffraction pattern is shown in Figure 1B. It can be clearly seen that the pattern was mainly composed of $\alpha'$-martensite, and the pattern of austenite was not obvious, indicating that its content is low and the main phase of the grains has transformed from austenite to martensite through strain-induced martensitic transformation. The TEM result indicates that a nanocrystalline layer consisting mainly of martensite was constructed on the surface of 304 austenite stainless steel through strain-induced martensitic transformation.

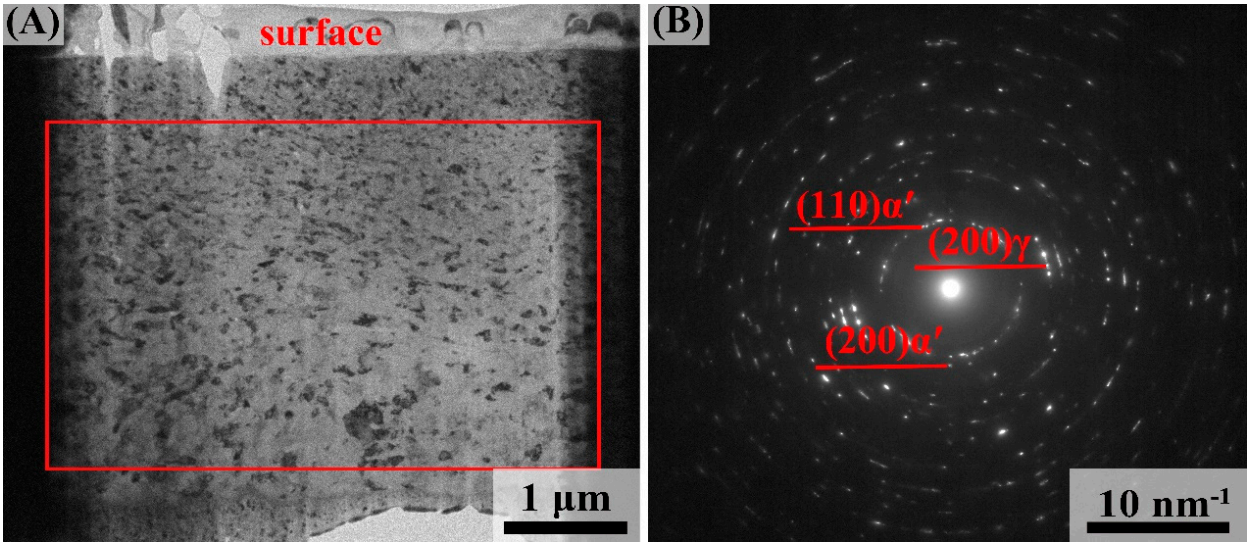


**Figure 1.** TEM characterization of the 304-Nano sample. (**A**) TEM images of specimens cut by FIB, (**B**) the corresponding selected area electron diffraction (SAED) patterns.

Due to the small size of the surface grains, it is difficult to accurately identify their grain size. Therefore, an area 1–3 μm away from the surface was selected to statistically analyze the grain size of the nanocrystalline layer, as shown in Figure 2. It can be seen that the grain size distribution of the nanocrystalline layer was between 40 and 340 nm, and the percentage of grains smaller than 100 nm was about 74%. The average grain size in the statistical area was also only around 89 nm. The result of the analysis revealed that the grain size of the nanocrystalline layer on the surface of 304 austenite stainless steel was within the expected range. Furthermore, the grain size was also found to be uniform across the layer. This indicates that the nanocrystalline layer on the surface of 304 austenite stainless steel was well-formed and homogeneous.

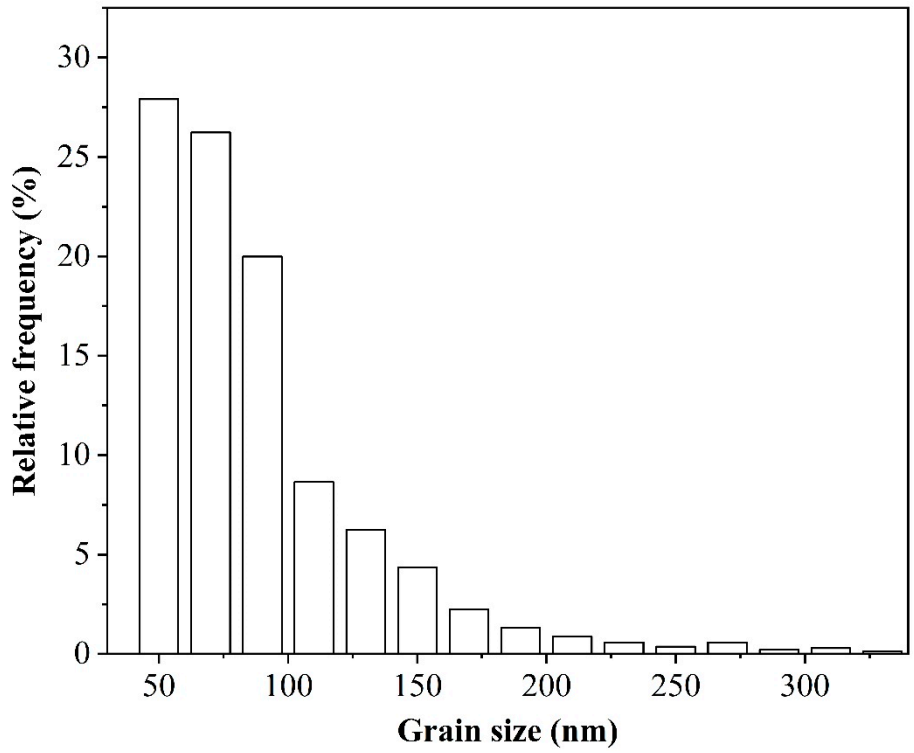


**Figure 2.** Grain distribution of the nanocrystalline layer on 304 stainless steel (selected area highlighted by red rectangle in Figure 1).

Since the strain-hardening ability of martensite is weaker than that of austenite during cavitation erosion [19,20], the martensite phase in the 304-Nano was partially conversely transformed into austenite by heat treatment, and two heat treatment temperatures (500 °C and 550 °C) were selected to adjust the phase content of the nanocrystalline layer. Figure 3 shows the XRD patterns of 304, 304-Nano, N-500 °C and N-550 °C samples. The 304 sample exhibited typical austenite peaks, which was consistent with previous studies [23,24]. After deformation processing, additional peaks appeared in the XRD pattern, identified as martensite peaks [25,26], which was consistent with the TEM result (Figure 1). Heat treatment at 500 °C and 550 °C did not trigger new peaks, and the peaks remained as austenite and martensite phases. It should be noted that the integrated intensity of the (111) and (220) planes of austenite and the (110) plane of martensite changed significantly at a heat treatment temperature of 500 °C, and this change was more noticeable when the heat treatment temperature raised from 500 to 550 °C. Furthermore, when the heat treatment temperature was 500 °C, the diffraction peaks (200)$\gamma$, (220)$\gamma$, (110)$\alpha'$, (200)$\alpha'$, and (211)$\alpha'$ had a significant shift to the right compared to those of the 304-Nano. However, these five peaks did not shift further when the temperature increased to 550 °C. In addition, except for a few martensite peaks, the three austenite peaks (111), (200), and (220) at N-500 °C and N-550 °C did not shift relative to the 304. According to Bragg's equation [27], residual tensile stress existed in the 304 formed by cutting processing of the 304-Nano, which was eliminated after heat treatment (N-500 °C and N-550 °C), causing the diffraction peaks to return to their corresponding angles. Based on the XRD diffraction result, the phase composition of the samples with different heat treatment temperatures was calculated and presented in Table 1. After strain treatment, some of the austenite was transformed into martensite in the 304-Nano. With increasing temperature, the austenite content began to increase, while the martensite content decreased. It has been reported that nano-grained 304 stainless steel could be prepared by equal-channel angular pressing (ECAP), and its strength and ductility could be balanced through heat treatment [28]. The grain size of 304 stainless steel grains with a size of 50 μm could be refined to 80–100 nm through strain treatment, and the grain size could still be maintained at 100–150 nm below

650 °C heat treatment. This was due to the fact that the grain has only undergone recovery and not recrystallization when the heat treatment is below 650 °C [29]. It has been suggested that the existence of martensite regions at triple junctions of reverted austenite might inhibit the further growth of austenite grains [30], which may result in ultrafine grains in reverse transformation austenite [31,32]. Thus, this study successfully produced a nanocrystalline layer on the surface of 304 stainless steel and achieved a biphasic regulation of the nanocrystalline layer through two different heat treatment temperatures.

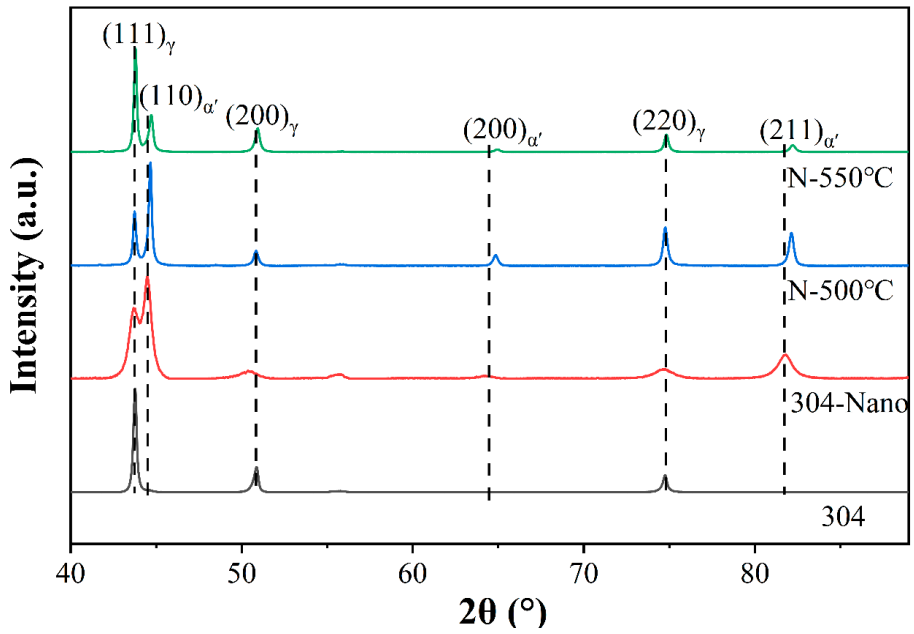


**Figure 3.** XRD pattern of the 304, 304-Nano, N-500 °C and N-550 °C samples.

**Table 1.** The percentage of austenite and martensite content in the 304, 304-Nano, N-500 °C and N-550 °C samples.

| Samples | Austenite (%) | Martensite (%) |
|---|---|---|
| 304 | 100 | 0 |
| 304-Nano | 35.3 ± 0.4 | 64.7 ± 0.4 |
| N-500 °C | 51.0 ± 2.8 | 49.0 ± 2.8 |
| N-550 °C | 67.8 ± 4.5 | 32.2 ± 4.5 |

Figure 4 shows the Vickers hardness of the 304, 304-Nano, N-500 °C and N-550 °C samples. It is clear that the Vickers hardness of the 304 sample was only 227 ± 3 $HV_{0.1}$, while after the cutting process, the Vickers hardness of the 304-Nano sample reached as high as 595 ± 18 $HV_{0.1}$, indicating a hardness increase of 106%. However, after the heat treatment at N-500 °C and N-550 °C, the hardness decreased to 521 ± 15 $HV_{0.1}$ and 433 ± 10 $HV_{0.1}$, respectively. Firstly, for the 304-Nano sample, on the one hand, the increase in hardness might be due to grain refinement, where smaller grain size led to higher hardness [33,34]; on the other hand, during the cutting process, martensitic transformation occurred where the hardness of martensite was greater than that of austenite [35,36]. Secondly, for the N-500 °C and N-550 °C samples, although the heat treatment process eliminated the tensile residual stress in the nanocrystalline layer, which might improve the hardness of nanocrystalline [37], the heat treatment process was accompanied by the transformation of martensite phase to austenite phase. A higher heat treatment temperature resulted in a greater decrease in hardness. The differences in hardness could affect the cavitation erosion resistance of a material.

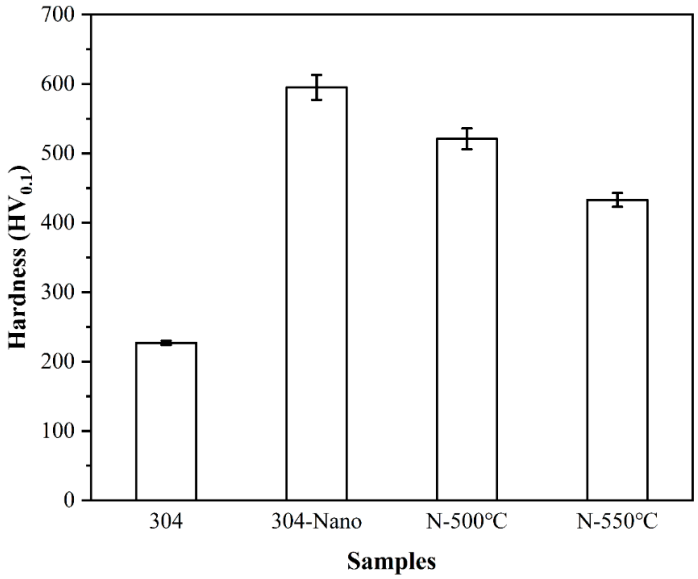


**Figure 4.** Vickers hardness of the 304, 304-Nano, N-500 °C and N-550 °C samples.

Figure 5A shows that the 304 sample had a cumulative mass loss of approximately 23.1 mg after 15 h of cavitation erosion, while the 304-Nano sample only had a cumulative mass loss of approximately 3.4 mg. After heat treatment, the cumulative mass loss of the N-500 °C and N-550 °C samples increased significantly to approximately 5.8 mg and 8.3 mg, respectively. In order to find the reasons for the differences in cumulative mass loss among the four samples, a clearer understanding of the mass loss during each stage is needed. Figure 5B shows the average mass loss rate curves of the four samples, from which it can be seen that the incubation period of the 304 sample was 3 h, gradually reaching the steady period through acceleration by 2 h, with a mass loss rate of approximately 2.0 mg/h during the steady period. In contrast, the 304-Nano sample had a prolonged incubation period of 6 h and an acceleration period of 7 h with a significantly lower mass loss rate during the acceleration period of the 304 sample. After entering the steady period, the mass loss rate of the 304-Nano sample was only approximately 0.4 mg/h. However, after heat treatment, the mass loss rates of the two samples treated at different temperatures exhibited different trends. The N-500 °C and N-550 °C samples both had an incubation period of 6 h, which was shorter than that of the 304-Nano sample. At this time, the difference in mass loss among the three was not significant. After entering the acceleration period, the acceleration period of the N-500 °C sample was maintained at 7 h, while that of the N-550 °C sample was only 5 h. After entering the steady period, the mass loss rates of the two samples were approximately 0.9 mg/h and 1.0 mg/h, respectively, which were much higher than that of the 304-Nano sample. The differences in the duration of different periods led to differences in the mass loss of the four samples. Furthermore, the average mass loss rates of the four samples during the acceleration period were, in order from largest to smallest: 304, N-550 °C, N-500 °C, and 304-Nano samples, respectively. This difference during the acceleration period was the main reason for the differences in cumulative mass loss among the four samples. After heat treatment, the austenite phase content in the N-500 °C and N-550 °C samples increased significantly to 51.0 ± 2.8% and 67.8 ± 4.5%, respectively, which was much higher than the austenite content in the 304-Nano sample (35.3 ± 0.4%). Generally, the hardness of austenite is lower than that of martensite [35,36], which means that an increase in the austenite phase content will decrease the hardness of the sample. After heat treatment, the hardness values of the two samples were 521 ± 15 $HV_{0.1}$ (N-500 °C) and 433 ± 10 $HV_{0.1}$ (N-550 °C), respectively. The Vickers hardness of the N-500 °C was 20.3% higher than that of the N-550 °C, which was consistent with the trend in the change of austenite phase content. During the cavitation erosion test, the hardness of the sample has a significant effect on its resistance to cavitation erosion. Previous studies have shown that increasing the hardness of the material could significantly enhance its ability to resist cavitation damage [38–40]. In this study, the

hardness of the N-500 °C sample (521 ± 15 $HV_{0.1}$) was much higher than that of the N-550 °C sample (433 ± 10 $HV_{0.1}$), which might be the reason why the N-500 °C sample exhibited higher resistance to cavitation erosion than the N-550 °C sample.

Residual stress can be classified into tensile residual stress and compressive residual stress. It was reported that both compressive and tensile residual stresses had a significant effect on the cavitation erosion resistance of the materials. Anatolii et al. applied alternating magnetic field treatment to EN8 steel and nickel–aluminum bronze alloy, which resulted in the generation of compressive residual stress in the treated samples [41]. The results showed a significant improvement in the cavitation erosion resistance of the samples with compressive residual stress. Other studies have also demonstrated that compressive residual stress could improve the cavitation erosion resistance of the materials [13,42]. Pedzich et al. investigated the influence of tensile residual stress on the cavitation erosion behavior of alumina–tungsten carbide composite ceramics. The results showed that tensile residual stress significantly reduced the cavitation erosion resistance of the composite ceramics [43]. The above studies indicated that tensile residual stress decreased the resistance of the materials to cavitation erosion, while compressive residual stress enhanced the ability of the materials to resist cavitation erosion damage. In this study, the austenite peak ((200) crystal plane) of the 304-Nano sample showed a significant left shift (compared to the original 304 sample), indicating the presence of tensile residual stress [27]. After heat treatment, the austenite peak ((200) crystal plane) of the samples (N-500 °C and N-550 °C) returned to the original position (compared to the original 304 sample), indicating the release of tensile stress, which was beneficial for resisting erosion damage. However, heat treatment increased the austenite phase content, resulting in a significant decrease in the Vickers hardness of the sample. The decrease in hardness was unfavorable for resisting erosion damage; therefore, the cavitation erosion resistance of the heat-treated samples (N-500 °C and N-550 °C) was reduced.

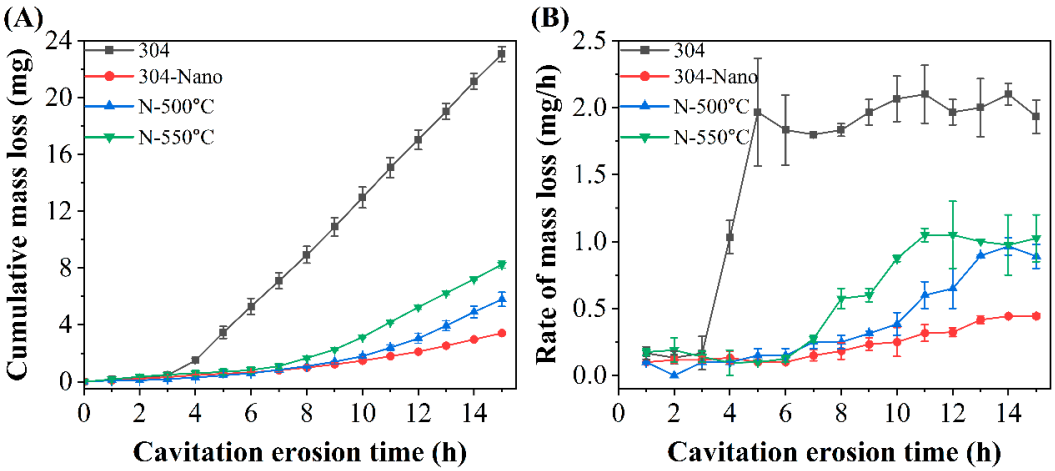


**Figure 5.** Cumulative mass loss (**A**) and rate of mass loss (**B**) of the 304, 304-Nano, N-500 °C and N-550 °C samples exposed to cavitation erosion in deionized water for 15 h.

Figure 6 depicts the 3D surface morphology (−1) and pit depth distribution statistics (−2) of the 304, 304-Nano, N-500 °C and N-550 °C samples after 15 h of cavitation erosion in deionized water. Sa, the surface roughness after cavitation erosion was analyzed based on the 3D surface morphology in order from largest to smallest: 304, N-550 °C, N-500 °C, and 304-Nano. Typically, the more damaged a sample is during the cavitation erosion process, the rougher its surface becomes after cavitation erosion. Additionally, by analyzing the pit depth distribution statistically on the surfaces of the four samples after cavitation erosion, the 304 sample had a pit depth distribution at 0–37.6 μm, while the 304-Nano sample had a pit depth distribution at 0–18.9 μm. After heat treatment, the pit depth distributions of the N-500 °C and N-550 °C samples were 0–21.7 μm and 0–22.9 μm, respectively. The results suggest that cavitation erosion pit growth in the 304-Nano sample was

inhibited, and this inhibition effect was weakened significantly after heat treatment. Moreover, the inhibitory effect was more pronounced with increasing heat treatment temperature. This explains why the 304-Nano sample exhibited exceptional cavitation erosion resistance, but its performance deteriorated after heat treatment and gradually weakened with an increasing heat treatment temperature.

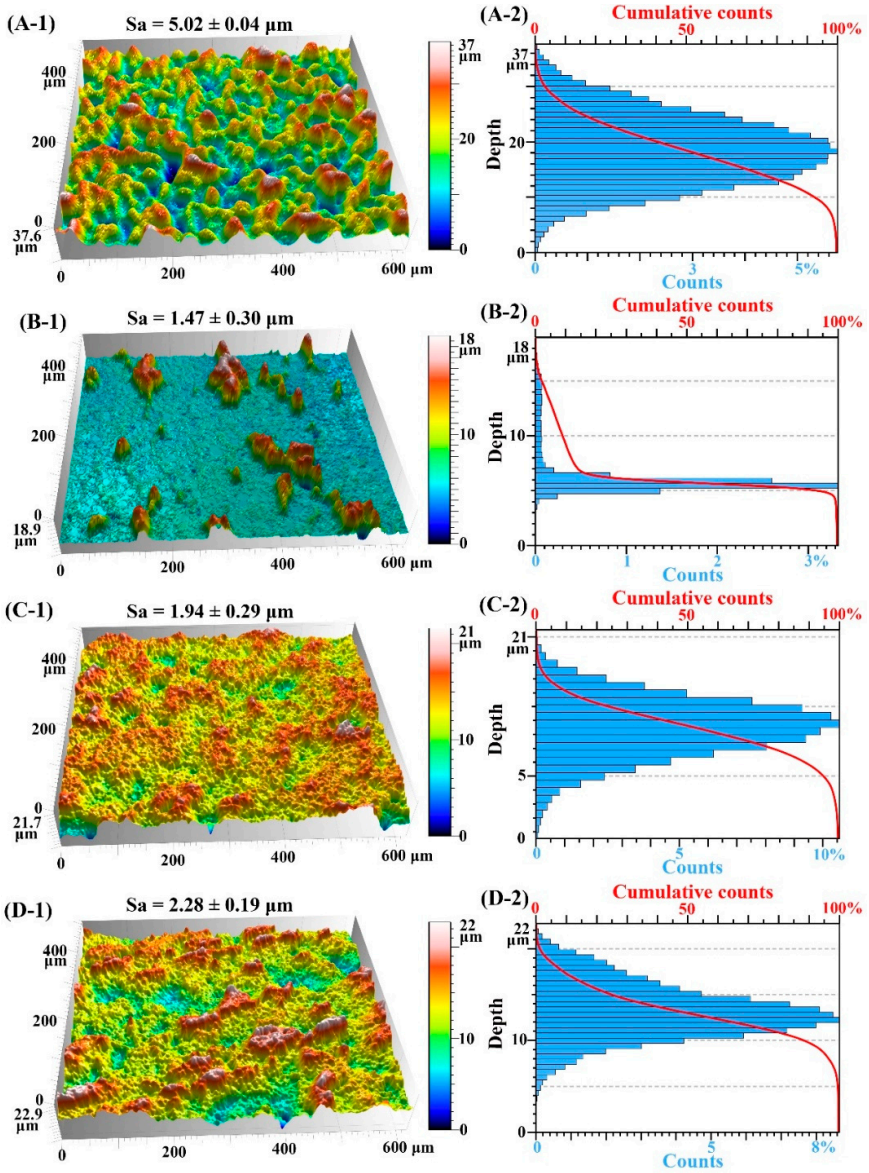


**Figure 6.** Three-dimensional (3D) surfaces topography (−1) and depth distribution on the eroded surface (−2) of the 304 (**A**), 304-Nano (**B**), N-500 °C (**C**) and N-550 °C samples (**D**) after cavitation erosion in deionized water for 15 h.

Figure 7 illustrates the 2D surface morphology (−1) of the samples after cavitation erosion. The deep blue to black regions represents erosion pits, and the more erosion pits there were, the more severe the surface damage. Figure 7 (A-2, B-2, C-2 & D-2) corresponds to the linear surface profile marked by the horizontal lines in Figure 7 (A-1, B-1, C-1 & D-1), with Ra values representing the ups and downs of pits on the lines. It was observed that the pit ups and downs of the 304-Nano, N-500 °C, and N-550 °C samples were relatively smoother than those of the 304 sample. This difference in the form of sample detachment might have caused the difference. After heat treatment, the surfaces became smoother, which could be due to the significant differences in surface morphology after erosion. Nevertheless, further observation of the surface morphology after erosion is required.

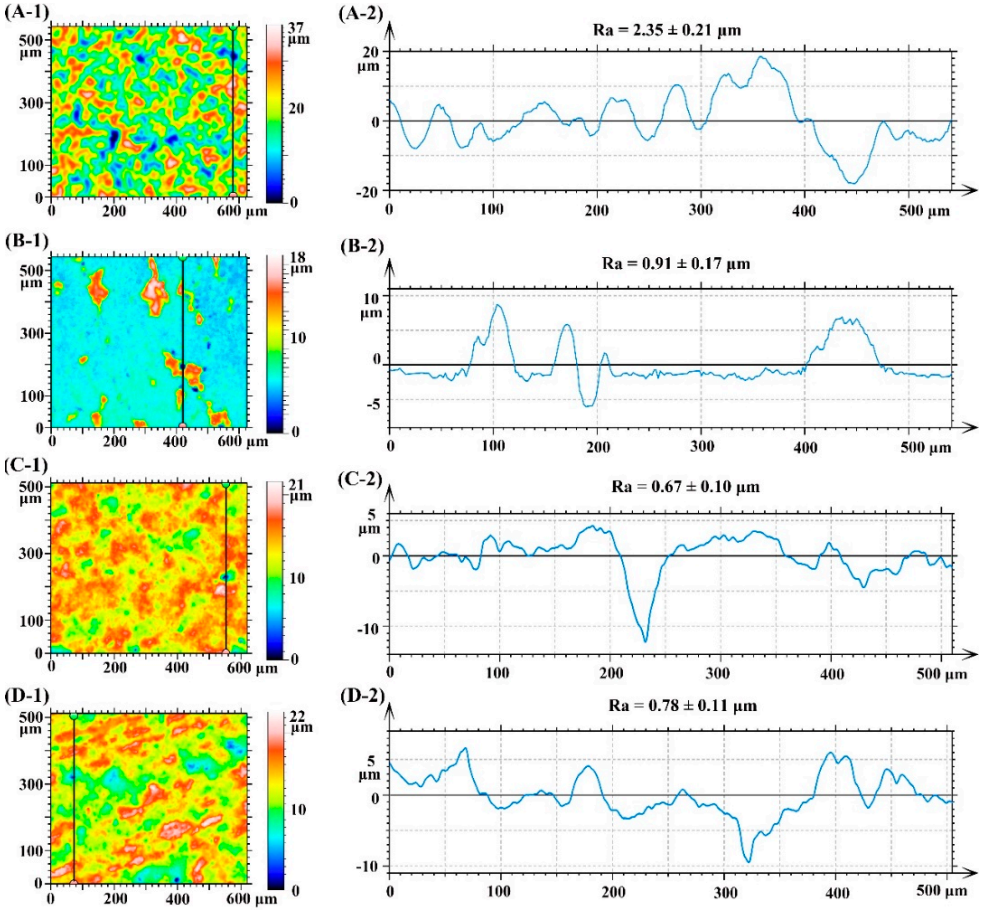


**Figure 7.** Surface profiles (−1) and linear profiles (−2) of the 304 (**A**), 304-Nano (**B**), N-500 °C (**C**) and N-550 °C samples (**D**) after cavitation erosion in deionized water for 15 h.

Figure 8 illustrates the SEM surface morphology of the 304, 304-Nano, N-500 °C and N-550 °C samples after 15 h of cavitation erosion in deionized water. As seen in Figure 8(A-1), the surface of the 304 sample was severely damaged and uneven, making the initial surface morphology unobservable. The growth of cracks around the cavitation pit, including small amounts of large cracks, was observed (Figure 8(A-2)). While for the 304-Nano, N-500 °C and N-550 °C samples, part of the original surface remained undamaged after cavitation erosion ((highlighted by the red arrow in Figure 8 (A-1, B-1, C-1 & D-1)), and the cracks near the pit were finer but more dispersed (highlighted by the red arrow in Figure 8 (A-2, B-2, C-2 & D-2)). Compared with the N-500 °C sample, the surface cracks of the N-550 °C sample become even larger after cavitation erosion. In general, the more dispersed and finer the cracks, the stronger the ability to inhibit crack propagation, resulting in less mass loss. This indirectly indicates that the anti-cavitation erosion ability of the 304-Nano sample was weakened by heat treatment, and this effect became more pronounced with the increasing heat treatment temperature. From the observation of the surface morphology after cavitation erosion of the four samples, it can be inferred that the anti-cavitation erosion performance of the samples may be related to their grain size and hardness. First of all, the deformation-induced martensitic nanocrystals will not undergo a recrystallization process below 650 °C during heat treatment [28,29]. Therefore, it can be assumed that the grain size of the 304-Nano, N-500 °C and N-550 °C samples remain basically unchanged and all were nano-crystals. Nano-crystals have an ultra-high density of grain boundaries, and the dislocations formed during cavitation erosion will slip to the grain boundaries, causing stress concentration at the grain boundaries. Stress accumulation was more difficult with the increase in grain boundaries, which slowed down the propagation of cracks [44,45]. This explains why the anti-cavitation erosion performances of the 304-Nano, N-500 °C and N-550 °C samples were significantly better than that of the 304

sample. Secondly, due to the transformation of martensite to austenite after heat treatment, the hardness of the N-500 °C and N-550 °C samples decrease relative to the 304-Nano sample, and the decrease was greater with increasing temperature. This led to a decrease in the ability of the N-500 °C and N-550 °C samples to resist the energy impact of cavitation erosion, which explains why the anti-cavitation erosion ability of the samples decreases after heat treatment, and this effect became more pronounced with increasing temperature.

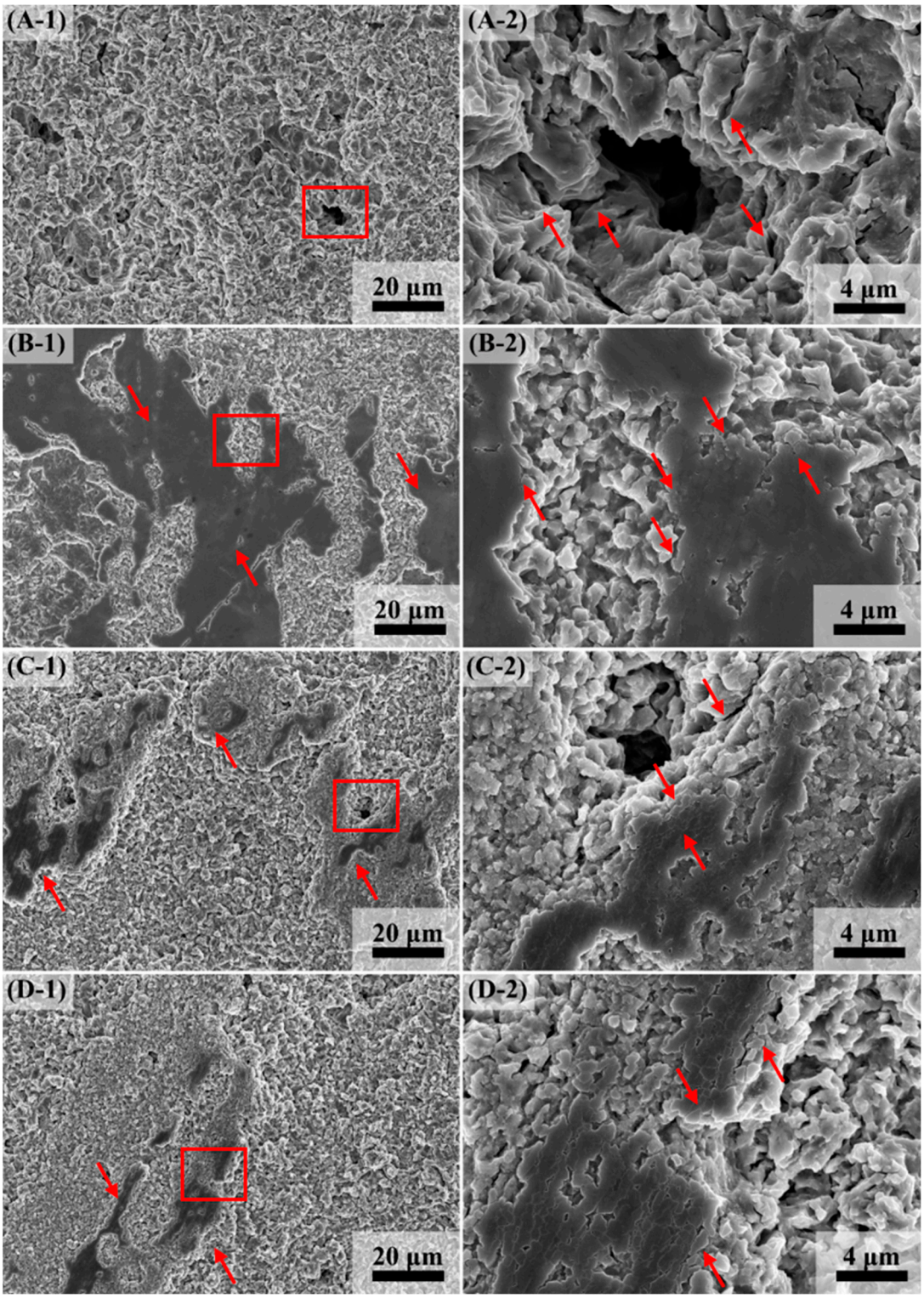


**Figure 8.** SEM images of the 304 (**A**), 304-Nano (**B**), N-500 °C (**C**) and N-550 °C (**D**) samples after cavitation erosion in deionized water for 15 h.

## 4. Conclusions

This study was based on the principle of deformation-induced martensitic transformation in austenitic stainless steel, and a nano-crystalline layer dominated by the martensitic phase was constructed on the surface of 304 stainless steel. The diphasic control of the nanocrystalline layer was carried out by heat treatment (500 and 550 °C), and the anti-cavitation erosion performance of the nanocrystalline layer before and after heat treatment was studied. The following conclusions can be drawn:

1. The Vickers hardness of the nanocrystalline layer is as high as 595 ± 18 $HV_{0.1}$, and after heat treatment at 500 and 550 °C, the Vickers hardness decreases to 521 ± 15 $HV_{0.1}$ and 433 ± 10 $HV_{0.1}$, respectively. This may be due to the reverse transformation of austenite.
2. The cumulative mass loss of the 304-Nano, N-500 °C, and N-550 °C samples in deionized water are 1/7, 1/5, and 1/3 of that of the 304 sample, respectively. This may be related to its ultra-high density grain boundaries of the nanocrystalline layer.
3. The reduction in hardness is the main reason for the decrease in the cavitation erosion resistance of the nanocrystalline layers after heat treatment.

**Author Contributions:** All authors have read and agreed to the published version of the manuscript. Methodology, N.H.; Investigation, N.H.; Writing-original draft, N.H., Y.T.; Writing-review & editing, Y.T., R.Y., X.C.; Conceptualization, X.C.; Supervision, H.L., T.X., X.C.

**Funding:** This research was funded by the Zhejiang Provincial Natural Science Foundation of China (grant #LZ22E090001), and Ningbo 3315 Talents Program (grant #2020A-29-G).

**Institutional Review Board Statement:** Not applicable.

**Informed Consent Statement:** Not applicable.

**Data Availability Statement:** All data are available in the main text or the supplementary materials.

**Acknowledgments:** Not applicable.

**Conflicts of Interest:** The authors declare no conflict of interest.

## Reference

1. Aktas, B.; Usta, O.; Atlar, M. Systematic investigation of coating application methods and soft paint types to detect cavitation erosion on marine propellers. *Appl. Ocean Res.* **2020**, *94*, 101868.
2. Nagaya, Y.; Murase, M.; Mizuyama, S.; Hattori, S. Evaluation of Incipient Cavitation Erosion on Pipe Walls Downstream from an Orifice. *J. Environ. Eng.* **2010**, *5*, 389–401.
3. ČDina, M. Detection of Cavitation Phenomenon in a Centrifugal Pump Using Audible Sound. *Mech. Syst. Signal Process* **2003**, *17*, 1335–1347.
4. Ferrari, A. Modelling approaches to acoustic cavitation in transmission pipelines. *Int. J. Heat Mass Transf.* **2010**, *53*, 4193–4203.
5. Liu, B.; Zhao, J.; Qian, J. Numerical analysis of cavitation erosion and particle erosion in butterfly valve. *Eng. Fail. Anal.* **2017**, *80*, 312–324.
6. Brennen, C.E. Cavitation Bubble Collapse. In *Cavitation and Bubble Dynamics*; Brennen, C.E., Ed.; Cambridge University Press: Cambridge, UK, 2013; pp. 59–88.
7. Matsumoto, Y.; Beylich, A.E. Influence of homogeneous condensation inside a small gas bubble on its pressure response. *J. Fluid Eng.* **1985**, *107*, 281–286.
8. Dular, M.; Bachert, B.; Stoffel, B.; Širok, B. Relationship between cavitation structures and cavitation damage. *Wear* **2004**, *257*, 1176–1184.
9. Tomlinson, W.J.; Talks, M.G. Laser surface processing and the cavitation erosion of a 16 wt.% Cr white cast iron. *Wear* **1990**, *139*, 269–284.
10. dos Santos, J.F.; Garzón, C.M.; Tschiptschin, A.P. Improvement of the cavitation erosion resistance of an AISI 304L austenitic stainless steel by high temperature gas nitriding. *Mater. Sci. Eng. A* **2004**, *382*, 378–386.
11. Zeng, S.; Hu, S.; Cheng, G. Effect of shot peening on surface characterization and cavitation resistance of nickel aluminum bronze. *Mater. Today Commun.* **2022**, *33*, 104767.
12. Mishra, R.S.; Ma, Z.Y. Friction stir welding and processing. *Mater. Sci. Eng. R* **2005**, *50*, 1–78.
13. Si, C.; Sun, W.; Tian, Y.; Cai, J. Cavitation erosion resistance enhancement of the surface modified 2024T351 Al alloy by ultrasonic shot peening. *Surf. Coat. Technol.* **2023**, *452*, 129122.
14. Thapliyal, S.; Dwivedi, D.K. On cavitation erosion behavior of friction stir processed surface of cast nickel aluminium bronze.

*Wear* **2017**, *376–377*, 1030–1042.
15. Selvam, K.; Mandal, P.; Grewal, H.S.; Arora, H.S. Ultrasonic cavitation erosion-corrosion behavior of friction stir processed stainless steel. *Ultrason. Sonochem.* **2018**, *44*, 331–339.
16. Escobar, J.D.; Velásquez, E.; Santos, T.F.A.; Ramirez, A.J.; López, D. Improvement of cavitation erosion resistance of a duplex stainless steel through friction stir processing (FSP). *Wear* **2013**, *297*, 998–1005.
17. Zhu, L.; Ruan, H.; Chen, A.; Guo, X.; Lu, J. Microstructures-based constitutive analysis for mechanical properties of gradient-nanostructured 304 stainless steels. *Acta Mater.* **2017**, *128*, 375–390.
18. Zhang, H.W.; Hei, Z.K.; Liu, G.; Lu, J.; Lu, K. Formation of nanostructured surface layer on AISI 304 stainless steel by means of surface mechanical attrition treatment. *Acta Mater.* **2003**, *51*, 1871–1881.
19. Liu, W.; Zheng, Y.G.; Liu, C.S.; Yao, Z.M.; Ke, W. Cavitation erosion behavior of Cr–Mn–N stainless steels in comparison with 0Cr13Ni5Mo stainless steel. *Wear* **2003**, *254*, 713–722.
20. Heathcock, C.J.; Protheroe, B.E.; Ball, A. Cavitation erosion of stainless steels. *Wear* **1982**, *81*, 311–327.
21. De, A.K.; Murdock, D.C.; Mataya, M.C.; Speer, J.G.; Matlock, D.K. Quantitative measurement of deformation-induced martensite in 304 stainless steel by X-ray diffraction. *Scr. Mater.* **2004**, *50*, 1445–1449.
22. Chahine, G.L.; Franc, J.P.; Karimi, A. Cavitation and cavitation Erosion. In *Advanced Experimental and Numerical Techniques for Cavitation Erosion Prediction*; Kim, K.-H., Chahine, G., Franc, J.-P., Karimi, A., Eds.; Springer: Dordrecht, The Netherlands 2014; pp. 3–20.
23. Kaoumi, D.; Liu, J. Deformation induced martensitic transformation in 304 austenitic stainless steel: In-situ vs. ex-situ transmission electron microscopy characterization. *Mater. Sci. Eng. A* **2018**, *715*, 73–82.
24. Eid, E.A.; Sadawy, M.M.; Reda, A.M. Computing the dynamic friction coefficient and evaluation of radiation shielding performance for AISI 304 stainless steel. *Mater. Chem. Phys.* **2022**, *277*, 125446.
25. Shen, Y.F.; Li, X.X.; Sun, X.; Wang, Y.D.; Zuo, L. Twinning and martensite in a 304 austenitic stainless steel. *Mater. Sci. Eng. A* **2012**, *552*, 514–522.
26. Zheng, Z.J.; Gao, Y.; Liu, J.W.; Zhu, M. A hybrid refining mechanism of microstructure of 304 stainless steel subjected to ECAP at 500 °C. *Mater. Sci. Eng. A* **2015**, *639*, 615–625.
27. Tian, Y.; Zhao, H.; Yang, R.; Liu, X.; Chen, X.; Qin, J.; McDonald, A.; Li, H. In-situ SEM investigation on stress-induced microstructure evolution of austenitic stainless steels subjected to cavitation erosion and cavitation erosion-corrosion. *Mater. Des.* **2022**, *213*, 110314.
28. Zheng, Z.J.; Liu, J.W.; Gao, Y. Achieving high strength and high ductility in 304 stainless steel through bi-modal microstructure prepared by post-ECAP annealing. *Mater. Sci. Eng. A* **2017**, *680*, 426–432.
29. Tsuji, N.; Ito, Y.; Saito, Y.; Minamino, Y. Strength and ductility of ultrafine grained aluminum and iron produced by ARB and annealing. *Scr. Mater.* **2002**, *47*, 893–899.
30. Tomimura, K.; Takaki, S.; Tokunaga, Y. Reversion Mechanism from Deformation Induced Martensite to Austenite in Metastable Austenitic Stainless Steels. *ISIJ Int.* **1991**, *31*, 1431–1437.
31. Souza Filho, I.R.; Almeida Junior, D.R.; Gauss, C.; Sandim, M.J.R.; Suzuki, P.A.; Sandim, H.R.Z. Austenite reversion in AISI 201 austenitic stainless steel evaluated via in situ synchrotron X-ray diffraction during slow continuous annealing. *Mater. Sci. Eng. A* **2019**, *755*, 267–277.
32. Misra, R.D.K.; Nayak, S.; Mali, S.A.; Shah, J.S.; Somani, M.C.; Karjalainen, L.P. On the Significance of Nature of Strain-Induced Martensite on Phase-Reversion-Induced Nanograined/Ultrafine-Grained Austenitic Stainless Steel. *Metall. Mater. Trans. A* **2010**, *41*, 3–12.
33. Yin, H.; Song, M.; Deng, P.; Li, L.; Prorok, B.C.; Lou, X. Thermal stability and microstructural evolution of additively manufactured 316L stainless steel by laser powder bed fusion at 500–800 °C. *Addit. Manuf.* **2021**, *41*, 101981.
34. Mai, Y.; Jie, X.; Liu, L.; Yu, N.; Zheng, X. Thermal stability of nanocrystalline layers fabricated by surface nanocrystallization. *Appl. Surf. Sci.* **2010**, *256*, 1972–1975.
35. Guimarães, J.R.C.; Maria, C.R. The Hardness of Martensite-Austenite Mixtures in Fe-31.9%Ni-0.02%C. *Mater. Sci. Eng.* **1980**, *43*, 55–58.
36. Mola, J.; Ren, M. On the hardness of high carbon ferrous martensite. *IOP Conf. Ser. Mater. Sci. Eng.* **2018**, *373*, 012004.
37. Sasahara, H. The effect on fatigue life of residual stress and surface hardness resulting from different cutting conditions of 0.45%C steel. *Int. J. Mach. Tool Manufact.* **2005**, *45*, 131–136.
38. Li, Y.; Lian, Y.; Sun, Y. Comparison of cavitation erosion behaviors between the as-cast and friction stir processed Ni–Al bronze in distilled water and artificial seawater. *J. Mater. Res. Technol.* **2021**, *13*, 906–918.
39. Raami, L.; Varis, T.; Valtonen, K.; Wendler, M.; Volkova, O.; Peura, P. Enhancing the cavitation erosion resistance of AISI 420-type stainless steel with quenching and partitioning. *Wear* **2023**, *526–527*, 204897.
40. Li, Z.X.; Zhang, L.M.; Ma, A.L.; Hu, J.X.; Zhang, S.; Daniel, E.F.; Zheng, Y.G. Comparative study on the cavitation erosion behavior of two different rolling surfaces on 304 stainless steel. *Tribol. Int.* **2021**, *159*, 106994.
41. Babutskyi, A.; Akram, S.; Bevilacqua, M.; Chrysanthou, A.; Montalvão, D.; Whiting, M.J.; Pizurova, N. Improvement of cavitation erosion resistance of structural metals by alternating magnetic field treatment. *Mater. Des.* **2023**, *226*, 111630.
42. Zhang, L.; Zhang, Y.K.; Lu, J.Z.; Dai, F.Z.; Feng, A.X.; Luo, K.Y.; Zhong, J.S.; Wang, Q.W.; Luo, M.; Qi, H. Effects of laser shock processing on electrochemical corrosion resistance of ANSI 304 stainless steel weldments after cavitation erosion. *Corros. Sci.* **2013**, *66*, 5–13.

43. Pędzich, Z.; Jasionowski, R.; Ziąbka, M. Cavitation wear of structural oxide ceramics and selected composite materials. *J. Eur. Ceram. Soc.* **2014**, *34*, 3351–3356.
44. Tian, Y.; Zhao, H.; Yang, R.; Zhang, H.; Yu, M.; Zhou, P.; Li, H.; Chen, X. Behavior of the hard phases of copper alloys subjected to cavitation erosion investigated by SEM observation. *Tribol. Int.* **2022**, *174*, 107771.
45. Zhang, L.M.; Ma, A.L.; Yu, H.; Umoh, A.J.; Zheng, Y.G. Correlation of microstructure with cavitation erosion behaviour of a nickel-aluminum bronze in simulated seawater. *Tribol. Int.* **2019**, *136*, 250–258.

**Disclaimer/Publisher's Note:** The statements, opinions and data contained in all publications are solely those of the individual author(s) and contributor(s) and not of MDPI and/or the editor(s). MDPI and/or the editor(s) disclaim responsibility for any injury to people or property resulting from any ideas, methods, instructions or products referred to in the content.